Three-Dimensional Imaging of the Structural Phase Transition in a Single Vanadium Dioxide Nanocrystal

Mansoor A. Najeeb*, Ahmed H. Mokhtar, David A. Serban, Daniel G. Porter, Steve Collins, Alessandro Bombardi, Marcus C. Newton

Mansoor A. Najeeb, Ahmed H. Mokhtar, David A. Serban, Marcus C. Newton
Department of Physics & Astronomy, University of Southampton, United Kingdom.
Email Address: [m.nellikkal@soton.ac.uk, m.c.newton@soton.ac.uk]
Daniel G. Porter, Steve Collins, Alessandro Bombardi
Diamond Light Source, Harwell Oxford Campus, Didcot, United Kingdom.

Vanadium dioxide (VO_2) is a strongly correlated material that exhibits a number of structural phase transitions (SPT) near to room temperature of considerable utility for various technological applications. When reduced to the nanoscale, a foreknowledge of surface and interface properties in VO_2 during the SPT can facilitate the development of devices based on VO_2. Here we show that Bragg Coherent X-ray Diffractive Imaging (BCDI) combined with machine learning is an effective means to recover three-dimensional images of a single VO_2 nanocrystal during a temperature-induced SPT from a room temperature monoclinic phase to a high-temperature rutile phase. Our findings reveal the coexistence of multiple phases within the nanocrystal throughout the transition, along with missing density which indicates the presence of a newly formed rutile phase.

1 Introduction

Direct observation of the origin and propagation of structural phase transition (SPT) in quantum materials is challenging due to their inherent complexity [1,2,3]. These challenges encompass dynamics from the atomic scale up to the macroscale and occur over timescales ranging from femtoseconds to microseconds. To capture the subtle changes in the atomic arrangements during the SPT can necessitate advanced analytical techniques like ultrafast electron diffraction (UED) [4,5,6], neutron scattering [7,8,9], and ultra-fast X-ray diffraction (UXRD) [10,11] with high spatial resolution capabilities. In the field of strongly correlated electronic materials [12,13,14] like high-temperature superconductors and transition metal oxides, the challenges of observing SPT are even more heightened due to the presence of competing phases, domain structures, and complex electronic interactions including strong electron-electron correlations coupling between charge, spin, orbital and lattice degrees of freedom [15,16,17,18,19,20,21].

A prototypical example of SPT in correlated materials is displayed by vanadium dioxide (VO_2), which exhibits a number of phase transitions, including a slow continuous SPT from a monoclinic (M1) to a monoclinic (M2) and an ultra-fast femtosecond symmetry-breaking SPT from M2 to rutile (R) just above the room temperature that is accompanied by a metal-to-insulator transition (MIT), spanning four orders of magnitude [22,16,23]. The SPT process is initiated at nucleation sites and defect regions [24] from which domains evolve depending on external factors like temperature [25], electric field [26], hydrostatic pressure [27], radiance [23], and applied deformation [28]. These changes propagate through the material as the phase transition progresses, leading to the formation of new crystal structures associated with different phases. Variation to the crystallographic phase within the material also influences the material's properties which enables them to be used in potential next-generation switching devices and other optoelectronic applications [29,30].

VO_2 can also exhibit various structures under different growth conditions, with the M1 and rutile R phases being the most common due to their reversible transition near room temperature. In the VO_2 R crystal structure, the V^{4+} ions occupy the body centre and the vertex of the tetragonal structure. Each V^{4+} ion, along with six surrounding O^{2-} ions, forms an octahedral VO_6 unit [16,31]. At the M1 phase, the vanadium ions are paired and arranged in a non-linear, non-parallel way across the octahedral edges, and with the somewhat disordered chains, the material behaves as an insulator [32]. The M2 phase which is formed as a result of a continuous transition has been also reported [33]. In the M2 phase which also has insulator properties, half of the vanadium ions form V-V dimers without rotating, whereas the other half of the vanadium ions exhibit a zigzag rotated pattern, while still maintaining an equidistant arrangement along the resulting zigzag chain [34]. The M1 phase has the V-O-V bond angle as 168 degrees [35] and while transitioning to the M2 phase the angle reduces to 162 degrees [33]. At the R
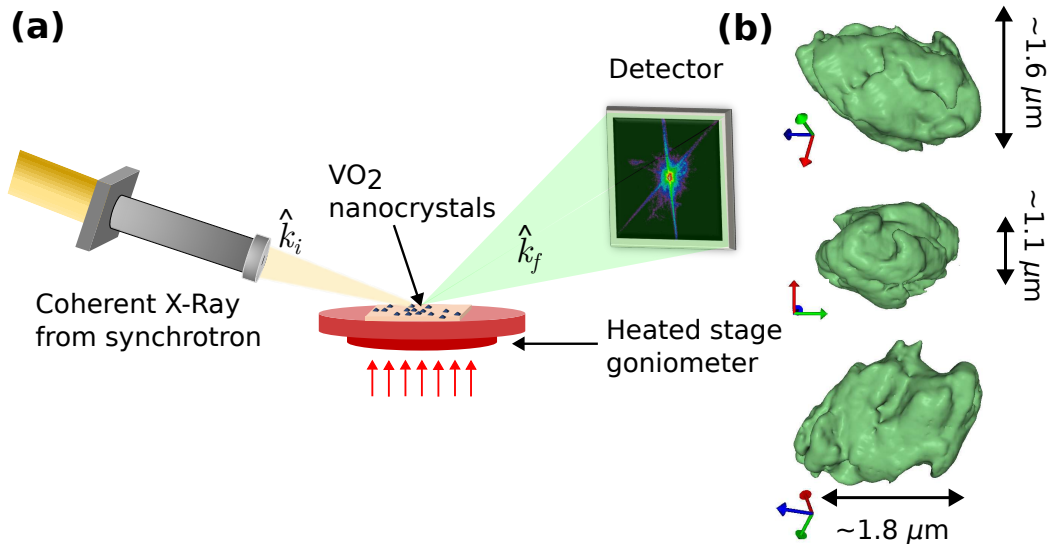
Figure 1: (a) Coherent Diffraction Imaging setup showing the incident ($\mathbf{k}_i$) and reflected ($\mathbf{k}_f$) X-ray wave vectors, (b) Reconstructed volume of a single VO_2 nanocrystal showing three orthogonal projections at an isosurface of 99.74%.

phase, the crystal structure becomes a higher symmetry, with well-defined arrangements of vanadium ions and a V-O-V bond angle of 90 degrees[36].

Despite numerous *in-situ* studies reported on M1 to R structural phase transition of VO_2 in thin-film form[1,37,38,39], there hasn't been reporting of a complete three-dimensional (3D) visualisation of the process in single VO_2 nanocrystals. Even though the conventional 2D ultra-fast characterisation techniques are capable of capturing the variations during SPT at an atomic level, they often miss the intricate details and spatial relationships crucial for understanding SPT. A 3D reconstruction of the captured signals into a comprehensible form overcomes these limitations by offering enhanced visualisation and data manipulation capabilities. In spite of the advantages of 3D image reconstruction, it is also often demanding due to the complexity of the crystal structure and the computational complexity involved in the reconstruction process.

Bragg Coherent X-ray Diffractive Imaging (BCDI) is a powerful tool that offers a 3D high-resolution image capturing for understanding complex phase transitions occurring in materials[40,41]. BCDI employs coherent X-rays to probe the internal structure of the materials at nanoscale, effectively revealing critical details that are often challenging to observe through conventional characterisation techniques. Notably non-destructive, BCDI offers clear insights into both surface and bulk strain characteristics of the material. The conventional methodology of BCDI involves the illumination of the sample with spatially coherent X-rays, where the coherence length surpasses the dimensions of the crystal[42,43]. In the Bragg reflection geometry, the entirety of the crystal volume scatters light, leading to corresponding interference patterns in the far field, thus producing a comprehensive 3D k-space diffraction pattern[44]. Subsequent to this, machine learning-aided iterative phase reconstruction methodologies are employed to recover the distinct 3D electron density and phase information[45,46]. The displacement of ions throughout the material correlates directly with the phase, enabling the derivation of strain information via the relationship $\phi = \mathbf{Q} \cdot \mathbf{u}$, where $\mathbf{u}$ represents atomic displacement[47,42]. In this study, we utilised BCDI to effectively capture SPT in a single VO_2 nanocrystal and used machine learning to successfully reconstruct the 3D images which display strong phase structure (i.e. $|\phi| \geq \frac{1}{2}\pi$) during temperature-induced M1 to R structural phase transition.

1.1 Methodology

BCDI characterisation was performed at Beamline I16 at the Diamond Light Source (DLS). The graphical representation of the BCDI experimental setup used is given in Figure 1a. A channel-cut Si (111) monochromator was used to produce a beam of 9 keV X-rays in Bragg geometry. The beam was then focused onto the sample mounted on a heated stage positioned at the eucentric point of the diffractometer. The heated stage incorporates calibrated diodes for accurate temperature monitoring during X-ray diffraction analysis. The sample was rotated

to locate the (011) reflection and diffraction data acquired using a QuadMerlin photon-counting area detector mounted in the reflection geometry. The sample was positioned 1,310 mm away from the detector. Rocking curve scans of range 16.7° to 18.9° at an increment of 0.01° and exposure time of 30 seconds were done. Measurements were taken at a range of temperatures from 320 K to 365 K from a single isolated VO_2 nanocrystal.

1.1.1   Machine learning model

Reconstructing the real-space images through iterative phase retrieval algorithms has been challenging for materials with a strong phase structure, mainly due to significant distortions in the speckle pattern[48,49]. We employed a deep learning model for phase retrieval based on a convolutional neural network (CNN) architecture[50]. Figure 2(a) illustrates the CNN used which uses an encoder-decoder framework, wherein the diffraction amplitude is first encoded into a feature space, then bifurcated into two branches for independent amplitude and phase recovery. The array size was reduced to half at every step in the encoder branch using Max Pool operations and the depth of the feature map was doubled using a convolution layer (Conv). The size of the output array was made to be half the size of the input diffraction pattern. Leaky LRLU activation function plus BN (Batch Normalisation) was used, for all the layers except for the last layer, where a ReLU (Rectified Linear Unit) function is used instead.

The network's training was conducted by the propagation of 25,000 simulated diffraction patterns through the network to generate predictions, which were then compared with the corresponding Fourier pair ground truth objects. The real space representation of each was characterised by a monoclinic object with dimensions that have random aspect ratios and a Gaussian-correlated phase profile, as derived in ref. 50. In contrast, the experimental data sourced from synchrotron facilities includes deviations from these ideal conditions, encompassing noise and variations in object dimensions and phase profiles, and lacks a predefined 'ground truth' for the real space image. The loss function, derived in ref. 50 and given by Eqn. 1, incorporated multiple terms, encompassing both real and Fourier spaces offering multiple parameters with which to monitor the network's performance. L_1 and L_2 represent losses for real space amplitude and phase, respectively. Additionally, L_3 leverages Fourier transforms of predictions to compute losses relative to input amplitudes. The relative weights of these functions are determined by integer parameters α_1, α_2, and α_3.

$$L_{\text{Train}} = \frac{1}{\alpha_1 + \alpha_2 + \alpha_3}[\alpha_1 L_1(\boldsymbol{A}_p, \boldsymbol{A}_g) + \alpha_2 L_2(\phi_p, \phi_g) + \alpha_3 L_3(\sqrt{I_p}, \sqrt{I_g})] \tag{1}$$

By utilizing back-propagation over at least 2000 epochs and implementing the ADAM (Adaptive Moment Estimation) optimizer[51], we attained a low and stable training loss. Subsequent to the initial training, we employed a transfer learning strategy, applying the pre-trained network to experimental diffraction patterns across several hundred epochs. The optimisation during this phase was guided by the loss metric comparing the Fourier transform of the predicted object against the provided diffraction pattern. This transfer learning phase enhances the model's robustness and provides a precise fine-tuning mechanism, making it more adaptable to specific data sets.

Figure 2(b) presents epoch versus training loss plot that illustrates the training progress of a machine learning model applied to the analysis. Each curve corresponds to a specific temperature, ranging from 320 K to 365 K, capturing the training loss over 2000 epochs. As the model undergoes training, the loss decreases, indicating improved convergence and enhanced performance in capturing the underlying patterns in the diffraction data. A low average training loss of 0.0329 (for data at 345 K) suggests that the machine learning model achieves a particularly accurate representation of the observed diffraction patterns at this temperature. For data at 365 K, the average training error loss was 0.0807. The low error loss across all the reconstructions indicates that the predicted output closely matches the actual data, reflecting a high level of agreement.

1.2   Results and discussions

Figure 1(b) shows the machine learning model reconstructed 3D images of a single VO_2 nanocrystal at 320 K. The resulting reconstructed object exhibits dimensions of approximately 1.8 μm x 1.6 μm x 1.1 μm at a resolution of 20 nm, revealing distinguishable crystal facets and well-defined morphological features. The presence of clear
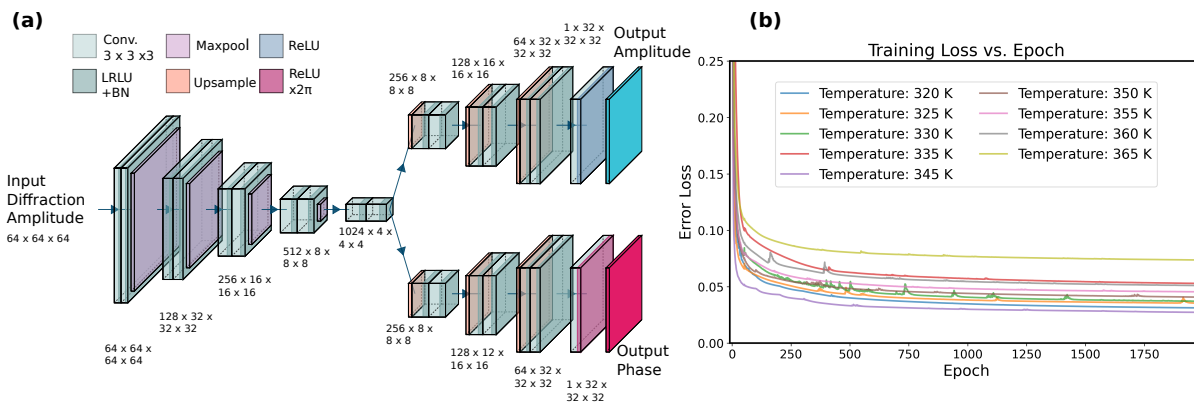
Figure 2: (a) Overview of the machine learning model used for the reconstruction of BCDI diffraction pattern. (b) Machine learning training loss plotted against the epoch iteration as the neural network model reconstructs the diffraction pattern for each of the nanocrystal under different temperatures. A low average training loss of 0.0329 was obtained for data 345 K.

and distinct facets imply an organised and ordered atomic arrangement within the crystal lattice, reflecting the crystalline nature of the material. Figure S3 (see supplementary material) shows the side-by-side comparison of the experimentally observed diffraction pattern and calculated Fourier transform of the resulting reconstruction for temperatures ranging from 320 K to 365 K. Good agreement is observed between the two and quantified in Table S2 (see supplementary material) as χ^2 error values.

The reconstructed electron density consists of phase and amplitude which correspond to the atomic displacements in the **Q**-vector direction and crystal morphology, respectively[52]. Figure 3 presents an overall view of the amplitude of the 3D reconstructed images of a single VO_2 nanocrystal at different temperatures. Notably, as the temperature increases from lower to higher values, the overall morphology of the reconstructed objects displays nuanced changes, while still retaining an average thickness of approximately 1.00 μm. At lower temperatures (320 K and 325 K), minimal morphological changes are observed. As previously stated, while transitioning to the M2 phase, the V-O-V bond angle reduces from 168 degrees[35] to 162 degrees[33]. This change in bond angle suggests a distortion in the crystal structure, which could potentially impact the crystal morphology. A critical transition temperature of 330 K - 335 K, marked by the solid-line box, signifies the onset of rapid transition of the crystal from the M2 to the R structure. This transition is associated with a slight increase in the density of the crystal when compared with the lower temperatures. More importantly, the SPT doesn't cease beyond the critical temperature, indicating multiple crystallographic phases within the nanocrystal. As the temperature rises (345 K - 355 K), we observe missing density in the reconstructed objects. This phenomenon may be attributed to the coexistence of monoclinic and rutile phases at elevated temperatures. This could be most likely smaller strain-induced grains forming within the crystallite, which no longer fulfill the Bragg condition. It is conceivable that these areas of the crystal diffract at different angles which results in missing Bragg electron density in those particular Bragg reflections and the detector may not capture this variation effectively[53].

Figure 4 shows the plotted maximum (ε_{max}), mean (ε_{mean}), and standard deviation (ε_{σ}) for the strain along the direction of the **Q**-vector for each temperature at different isosurface % during SPT. The maximum value shows the peak deformation experienced by the crystal at each temperature and the mean value shows the average strain magnitude across the diffraction pattern. Standard deviation shows the variation of strain magnitude within the crystal moving from a lower to higher isosurface area across various temperatures, reflecting the heterogeneity of strain across the different regions of the crystal. We observe a decrease in the standard deviation of strain as the isosurface % increases showing the strain difference between the surface and bulk of the crystal. This trend indicates that the core of the crystal experiences more substantial deformation during the SPT, likely due to the tightly constrained environment compared with the surface atoms with more degrees of freedom.

The SPT also gives rise to multiple crystallographic phase changes within the crystal. Exploring this variation solely through visual inspection of the reconstructed diffraction pattern across the temperature spectrum is challenging. In such scenarios, Principal Component Analysis (PCA) was used to provide a more systematic and insightful approach to uncovering the underlying structural intricacies and facilitating a comprehensive un-
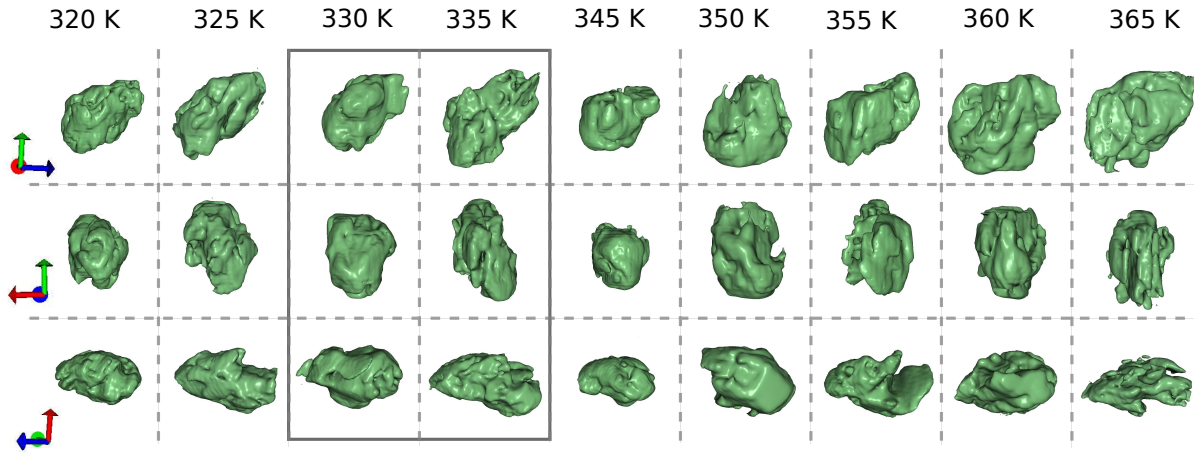
Figure 3: 3D reconstructed images of VO$_2$ nanocrystals showcasing amplitude which corresponds to the distinct crystal morphology at varying temperatures, displayed at three orthogonal angles visualised at an isosurface containing approximately 99.74% of the reciprocal data. The solid-line box highlights the critical transition temperature. The reconstructed objects corresponding to varying temperatures exhibit distinguishable crystal facets and well-defined morphological features.

derstanding of the phase transitions[54,55,56]. PCA was utilised to reduce the data dimensions and emphasise key features, thereby facilitating a more interpretable analysis. Additionally, PCA assists in identifying trends within the strain variation across the crystallographic phases with respect to varying temperatures, contributing to a better understanding of the phase transition dynamics. It is important to clarify that this concept is distinct from the order parameter in structural phase transition used in Landau theory[57,58]. The order parameter in PCA analysis of reconstructed diffraction patterns focuses on quantifying structural variation, while the order parameter in Landau theory describes the degree of order or symmetry in the system's macroscopic properties.

Initially, the reconstructed diffraction patterns were binned with dimensions (64, 64, 64) to reduce noise and computational complexity and then the phase information was extracted from the binned data. To identify the primary sources of structural variance across the temperature range, we computed the Covariance Matrix (C) using Eqn. 2. The covariance measures how changes in one variable correspond to changes in another. The covariance matrix was calculated by taking the outer product of the phase differences ($\Delta\phi_n = \phi_n - \phi_0$) for all temperature points, where ϕ_0 represents the phase at a reference temperature (here 320 K).

$$C = \sum_n (\Delta\phi_n \otimes \Delta\phi_n) \tag{2}$$

The subsequent stage involves conducting an eigenvalue-eigenvector decomposition of the covariance matrix C. This yields a set of eigenvalues (λ) and their corresponding eigenvectors ($\mathbf{v}$). The eigenvalues $C\mathbf{v} = \lambda\mathbf{v}$, represent the data variances along the principal components.

Principal components are determined from the eigenvectors. The first principal component is associated with the eigenvector corresponding to the largest eigenvalue (λ_1), the second principal component corresponds to the second-largest eigenvalue (λ_2), and so on. These principal components establish a basis for the data, explaining the maximum variance in decreasing order. The inner product of the phase information of the reconstructed object with the principal components was computed to project the original phase information into the new coordinate system defined by the principal components. This operation yields a set of values referred to as "order parameters" (O_i), quantifying the contribution of each diffraction pattern to the overall structural variation. The equation for calculating the PCA order parameters, O_i, is given by:

$$O_i = \mathbf{v}_i^T \cdot \Delta\phi_i \tag{3}$$

where $\mathbf{v}_i$ is the i-th eigenvector, with $\mathbf{v}_1$ being the leading eigenvector (first principal component). $\Delta\phi_i$ represents the phase differences of the diffraction patterns relative to the reference diffraction pattern. The leading principal component, associated with the largest eigenvalue (λ_1), encapsulates the most substantial structural variation. This equation highlights the concept of alignment between phase differences and principal components.
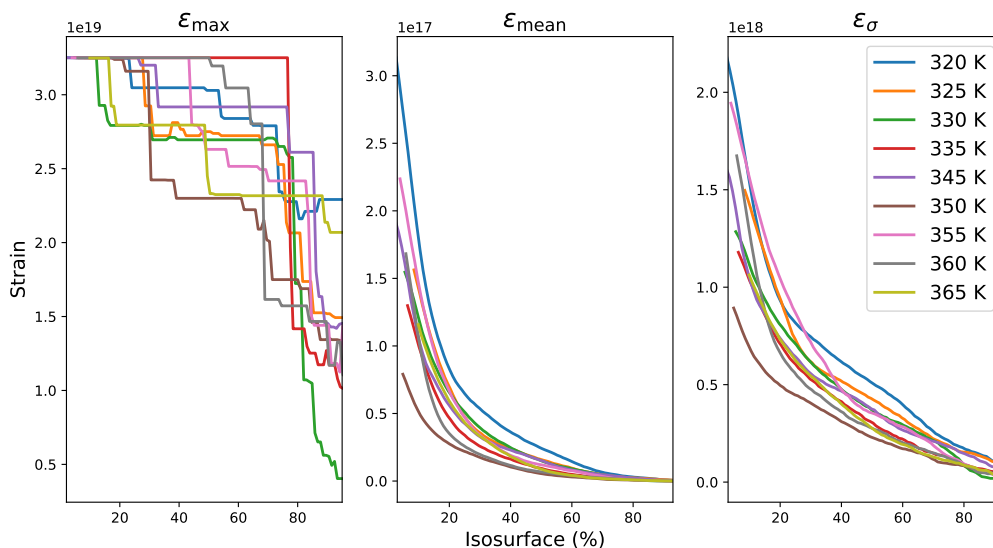
Figure 4: Max value (ε_{max}), mean value (ε_{mean}), and standard deviation (ε_{σ}) for the strain magnitude of a single VO$_2$ nanocrystal at various temperatures at different isosurface % during SPT. ε_{max} shows the peak deformation experienced by the crystal at each temperature and the ε_{mean} shows the average strain across the diffraction pattern. ε_{σ} shows the variation of strain across the crystal with respect to the temperature moving from a lower to higher isosurface area, reflecting the heterogeneity of strain across the different regions of the crystal.

The scree plot (Figure S1 of supplementary file) shows the eigenvalues from PCA analysis arranged from largest to smallest and Figure S2 shows the clustering of various temperatures across the first and second PCA components. While the order parameter was derived from a vector operation, for clarity the order parameter discussed here primarily refers to the projection onto the main principal components (single values corresponding to the main component), aligning with the largest eigenvalue (λ_1) of the covariance matrix. When phase differences align or are "parallel" to the leading eigenvector, the order parameter tends to yield larger values, indicating a strong contribution of the corresponding diffraction pattern to the overall structural variation. Conversely, when phase differences are orthogonal (perpendicular), the order parameter tends to yield zero values, suggesting minimal contribution of the diffraction pattern to the structural variation. Thus, the order parameters provide insights into the alignment between phase differences and the dominant structural features captured by PCA, facilitating the analysis of structural domain changes during the SPT.

To comprehensively understand the dynamic phase changes occurring within the crystal, we performed cross-sectional slicing of the reconstructed object along the x, y, and z axes. Figure 5(a) showcases the sliced images along the y-axis. The colour map shows the phase range of $-\pi$ and π displayed at the bottom of Figure 5(a) which is indicative of compressive and tensile strains respectively. At room temperature (320 K), a clear distinction between the tensile and compressive regions can be seen, showing a recognizable and organised pattern within the crystal structure. The presence of a positive phase (tensile strain) within the resting state (320 K) of the crystal, which was mostly visible on the surface region implies possible surface-induced effects, such as defects or imperfections, influencing strain localisation[59]. A significant change is observed at 325 K, where the positive phase which was initially surrounding the negative phase (compressive strain), rapidly spread across the crystal indicating the beginning of a M1 to M2 dynamic phase transition process. The compressive strain regions are shrunken into small islands (marked by arrows in Figure 5(a)), surrounded by the higher values of positive phase (violet colour) indicating the growth of M2 region in the vicinity of the island. A similar trend can be also seen in temperature 330 K of supplementary figures S3 and S4.

At 335 K, there is an overall shift from tensile strain to minimal compressive strain, indicated by the appearance of green phase regions, and the formation of localised neutral white regions which suggest a relaxation state. Missing density at 345 K occurs at surface regions that have likely transitioned to the rutile phase and no longer fulfill the Bragg condition. At 345 K and 350 K, islands of M2 phase persist. The occurrence of M2 regions at high temperatures confirms an inhomogeneous phase transition, where different regions of the material undergo
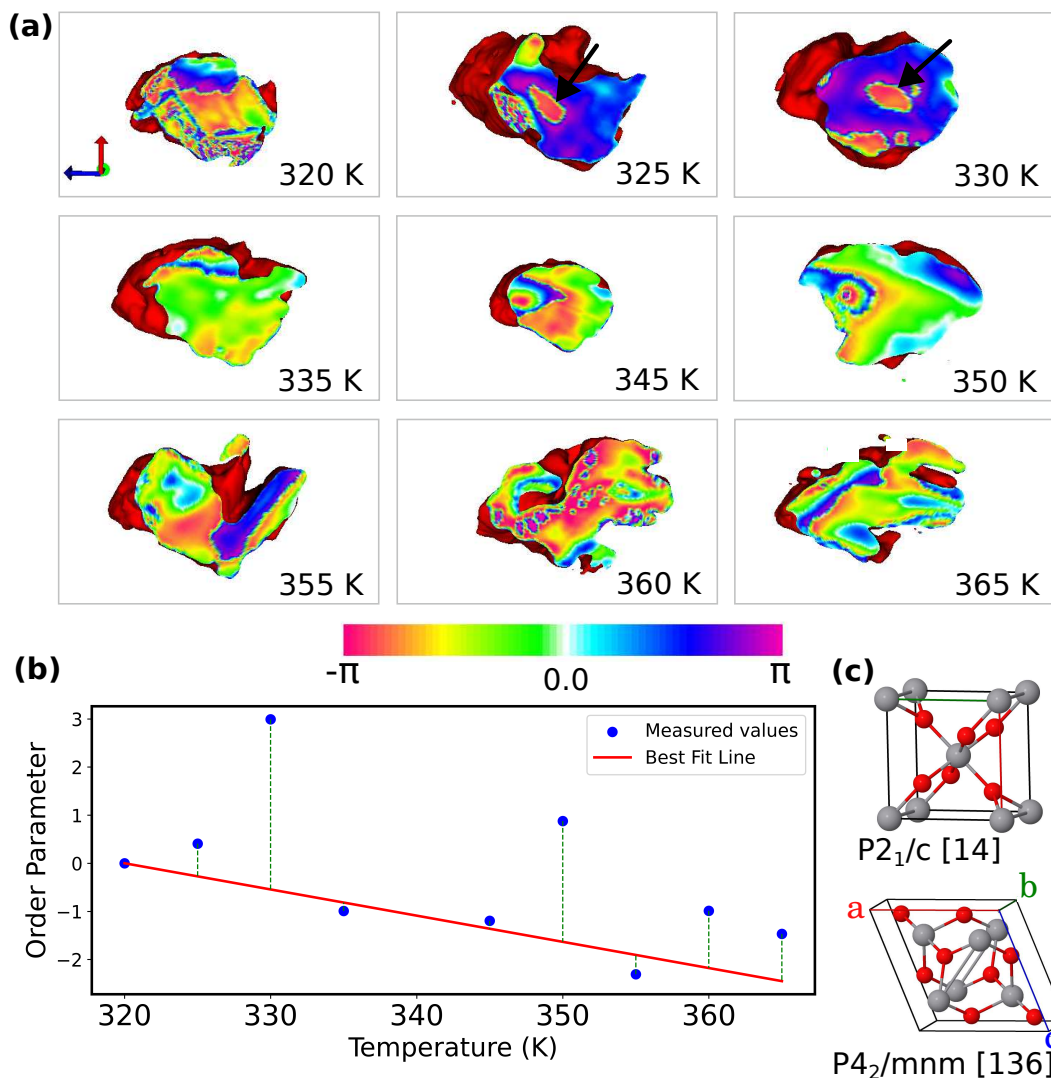
Figure 5: (a) Slices of reconstructed images (along the y-axis) showing the structural changes during phase transition at various temperatures. The $-\pi$ side of the color map indicates the compressive strain (green - red) and the π indicates the tensile strain (blue-violet). The areas highlighted with the arrow show a potential monoclinic M2 structure retained in this specific region. (b) PCA (Principal Component Analysis) of reconstructed diffraction pattern depicting the change in the order parameter with temperature. Blue scatter points represents measured order parameter values, the red line represents the best fit line and the error bar (dashed line) illustrates the difference between the actual and predicted values of the best fit line. (c) Crystal structures of monoclinic (M1) insulator phase and rutile (R) metallic phase.

transition at different rates, emphasizing the coexistence of crystallographic phases within the nanocrystal during SPT. These findings are consistent with our observations in the laboratory, and other reported findings[60,61,62,63] where optical microscopic studies of larger VO_2 crystals revealed different regions changing at different rates in response to the temperature. At 350 K the crystal retains a new organised pattern and as the temperature rises to 360 K, the majority of the system starts to settle with the new structural configuration. As the temperature reaches to 365 K, a further rearrangement in the phase profile was observed indicating the coexistence of crystal phases.

Figure 5(b) shows the PCA outcome by plotting the order parameter against each temperature. The order parameter of Eqn. 3 quantifies the degree of variation in phase, relative to the ground state throughout the nanocrystal during the structural phase transition. The blue scatter points represents actual measured order parameter values while the red line represents the best fitted line for the order parameter for corresponding temperatures. The error bar (dashed line) shows the variance between the measured data points and the corresponding predictions made by the best fit line. Table S1 (supplementary file) tabulates the numerical order parameter values and the best fitted values. At 320 K, the resting state of the crystal, the order parameter was zero as expected since it indicates a minimum deviation from the reference state of the crystal at room temperature. From 320 K to 330 k, the best

fit line represents the beginning of transition of the M1 phase ot a M2 phase. As the temperature further rises, the best fit line shows a decreasing trend in the order parameter indicative of the transition of the crystal moving away from the M1 phase to the M2 phase. At higher temperature, the order parameter shows oscillatory variations which are likely due to the co-existance of of M1, M2 and R phases. The compressive and tensile strain shown in Figure 5(a) and supplementary figures S3 and S4 also indicate the co-existance of multiple phases at higher temperature.

2 Conclusion

In this study, we show the complete 3D image reconstruction of VO_2 nanocrystal during a temperature-induced M1 to R transition. Cross-sectional analysis of the reconstructed object confirms the dynamics of the transition from a room-temperature M1 phase to a high-temperature R phase, displaying the coexistence of multiple phases within a single VO_2 nanocrystal throughout the transition which hasn't been previously achieved. We observed changes in crystal morphology with missing density likely caused by rutile regions that do not fulfill the mono-clinic Bragg condition. Our novel CNN model was found to be effective in robustly reconstructing the morphology and the strong phase structure inherent in the reconstructed objects due to the presence of tensile and compressive strains during SPT. An order parameter, derived using PCA was used to describe the structural evolution of the VO_2 nanocrystal and could be used to correlate the variations in phase distribution at which the transition from the distorted M1 phase to the more ordered R phase was initiated. Trends in the variation of phase information, as observed in the reconstructed VO_2 nanocrystal, are in good agreement with the PCA order parameter. The possibility of the coexistence of M2 and R phases at elevated temperatures is consistent with earlier findings, wherein localised and contrasted changes in reflectivity are observed under light microscope illumination in larger VO_2 nanocrystals during the structural phase transition.

3 Experimental Section

The VO_2 nanocrystals were synthesised by thermal chemical vapor deposition (CVD). A silicon (111) substrate of 10 mm x 10 mm, was used for the deposition. A custom-made tantalum mask with a pore size of 0.5 mm in diameter was used to control the crystallisation rate. Grounded VO_2 powder was placed in a quartz boat and the substrate was positioned upside-down and placed inside the furnace. The furnace was then heated to 800 °C while maintaining high vacuum conditions and argon gas flow at 3.0 sccm. The deposition time was set to 5 minutes and the furnace was cooled down to room temperature gradually. The growth substrates were then inspected with optical microscopy and micro-manipulation to transfer single well-faceted (011) plane VO_2 nanocrystals to a clean silicon substrate for synchrotron measurements.

Supporting Information

See the supplementary material for the χ^2 error values and a side-by-side comparison of the experimentally observed diffraction pattern and calculated Fourier transform of the resulting reconstruction along with the slices of reconstructed images showing the variations in the phase due to the structural domain changes during phase transition at various temperatures along the x axis and z axis.

Author Contributions

M.C.N. designed and supervised the study. All authors contributed to the BCDI experiment at D.L.S. A.H.M. and M.C.N. developed the machine learning model for the reconstruction of the BCDI pattern. M.C.N. and M.A.N. performed data reconstruction and analysis. M.A.N. wrote the manuscript with input from all authors.

Data Availability Statement

The data underpinning the findings of this study are available from M.C.N upon reasonable request. The computational analysis in this study utilized "Bonsu: The Interactive Phase Retrieval Suite" software package, and can be downloaded through PyPI (https://pypi.org/project/Bonsu/) or GitHub (https://github.com/bonsudev/bonsu).

Conflict of interest The authors have no conflicts to disclose.

References

[1] A. S. Johnson, D. Perez-Salinas, K. M. Siddiqui, S. Kim, S. Choi, K. Volckaert, P. E. Majchrzak, S. Ulstrup, N. Agarwal, K. Hallman, et al., *Nature Physics* **2023**, *19*, 2 215.

[2] J. O. Schunck, F. Döring, B. Rösner, J. Buck, R. Y. Engel, P. S. Miedema, S. K. Mahatha, M. Hoesch, A. Petraru, H. Kohlstedt, et al., *Scientific Reports* **2022**, *12*, 1 10464.

[3] J. Li, K. Sun, J. Li, Q. Meng, X. Fu, W.-G. Yin, D. Lu, Y. Li, M. Babzien, M. Fedurin, et al., *Applied Physics Letters* **2018**, *113*, 4.

[4] P. Baum, D.-S. Yang, A. H. Zewail, *science* **2007**, *318*, 5851 788.

[5] S. Ji, O. Grånäs, A. K. Prasad, J. Weissenrieder, *Nanoscale* **2023**, *15*, 1 304.

[6] A. Sood, X. Shen, Y. Shi, S. Kumar, S. J. Park, M. Zajac, Y. Sun, L.-Q. Chen, S. Ramanathan, X. Wang, et al., *Science* **2021**, *373*, 6552 352.

[7] Z. YAMANI, *Physics in Canada* **2018**, *74*, 1-2.

[8] X. Wang, Ph.D. thesis, Dissertation, RWTH Aachen University, 2021, **2021**.

[9] S. Guo, Y. Xu, T. Hoke, G. Sohi, S. Li, X. Chen, *Journal of Applied Physics* **2023**, *133*, 12.

[10] S. Wall, S. Yang, L. Vidas, M. Chollet, J. M. Glownia, M. Kozina, T. Katayama, T. Henighan, M. Jiang, T. A. Miller, et al., *Science* **2018**, *362*, 6414 572.

[11] H. Cailleau, E. Collet, M. B.-L. Cointe, M.-H. Lemée-Cailleau, S.-y. Koshihara, In *Photoinduced Phase Transitions*, 309–342. World Scientific, **2004**.

[12] J. Quintanilla, C. Hooley, *Physics World* **2009**, *22*, 06 32.

[13] P. W. Anderson, *Science* **1972**, *177*, 4047 393.

[14] D. N. Basov, R. D. Averitt, D. Van Der Marel, M. Dressel, K. Haule, *Reviews of Modern Physics* **2011**, *83*, 2 471.

[15] E. Dagotto, *Science* **2005**, *309*, 5732 257.

[16] Z. Shao, X. Cao, H. Luo, P. Jin, *NPG Asia Materials* **2018**, *10*, 7 581.

[17] G. Gou, I. Grinberg, A. M. Rappe, J. M. Rondinelli, *Physical Review B* **2011**, *84*, 14 144101.

[18] A. Grünebohm, A. Hütten, A. E. Böhmer, J. Frenzel, I. Eremin, R. Drautz, I. Ennen, L. Caron, T. Kuschel, F. Lechermann, et al., *Advanced Energy Materials* **2023**, *13*, 30 2300754.

[19] Y. Ren, *JOM* **2012**, *64* 140.

[20] A. Grünebohm, M. Marathe, R. Khachaturyan, R. Schiedung, D. C. Lupascu, V. V. Shvartsman, *Journal of Physics: Condensed Matter* **2021**, *34*, 7 073002.

[21] E. Dagotto, Y. Tokura, *Mrs Bulletin* **2008**, *33*, 11 1037.

[22] F. Morin, *Physical review letters* **1959**, *3*, 1 34.

[23] A. Cavalleri, T. Dekorsy, H. H. Chong, J.-C. Kieffer, R. W. Schoenlein, *Physical Review B* **2004**, *70*, 16 161102.

[24] J. Nag, R. F. Haglund, E. Andrew Payzant, K. L. More, *Journal of Applied Physics* **2012**, *112*, 10.

[25] J. Yoon, H. Kim, X. Chen, N. Tamura, B. S. Mun, C. Park, H. Ju, *ACS applied materials & interfaces* **2016**, *8*, 3 2280.

[26] H.-T. Kim, B.-G. Chae, D.-H. Youn, G. Kim, K.-Y. Kang, S.-J. Lee, K. Kim, Y.-S. Lim, *Applied Physics Letters* **2005**, *86*, 24.

[27] C. Marini, E. Arcangeletti, D. Di Castro, L. Baldassare, A. Perucchi, S. Lupi, L. Malavasi, L. Boeri, E. Pomjakushina, K. Conder, et al., *Physical Review B* **2008**, *77*, 23 235111.

[28] T. Kikuzuki, M. Lippmaa, *Applied Physics Letters* **2010**, *96*, 13.

[29] Y. J. Lee, K. Hong, K. Na, J. Yang, T. H. Lee, B. Kim, C. W. Bark, J. Y. Kim, S. H. Park, S. Lee, et al., *Advanced Materials* **2022**, *34*, 32 2203097.

[30] H.-W. Liu, W.-H. Liu, Z.-J. Suo, Z. Wang, J.-W. Luo, S.-S. Li, L.-W. Wang, *Proceedings of the National Academy of Sciences* **2022**, *119*, 28 e2122534119.

[31] Z. Yang, C. Ko, V. Balakrishnan, G. Gopalakrishnan, S. Ramanathan, *Physical Review B* **2010**, *82*, 20 205101.

[32] Y. Ji, Y. Zhang, M. Gao, Z. Yuan, Y. Xia, C. Jin, B. Tao, C. Chen, Q. Jia, Y. Lin, *Scientific reports* **2014**, *4*, 1 4854.

[33] M. Marezio, D. B. McWhan, J. Remeika, P. Dernier, *Physical Review B* **1972**, *5*, 7 2541.

[34] K. Nishikawa, M. Yoshimura, Y. Watanabe, *Journal of Vacuum Science & Technology A* **2022**, *40*, 3 033401.

[35] S. Xu, X. Shen, K. A. Hallman, R. F. Haglund Jr, S. T. Pantelides, *Physical Review B* **2017**, *95*, 12 125105.

[36] D. McWhan, M. Marezio, J. Remeika, P. Dernier, *Physical review B* **1974**, *10*, 2 490.

[37] V. Théry, A. Boulle, A. Crunteanu, J.-C. Orlianges, A. Beaumont, R. Mayet, A. Mennai, F. Cosset, A. Bessaudou, M. Fabert, *Physical Review B* **2016**, *93*, 18 184106.

[38] L. Rodríguez, F. Sandiumenge, C. Frontera, J. M. Caicedo, J. Padilla, G. Catalán, J. Santiso, *Acta Materialia* **2021**, *220* 117336.

[39] M. Kumar, S. Rani, J. P. Singh, K. H. Chae, Y. Kim, J. Park, H. H. Lee, *Applied Surface Science* **2020**, *529* 147093.

[40] X. Shi, J. Shi, E. Fohtung, *Journal of Applied Physics* **2022**, *131*, 4.

[41] R. Harder, I. K. Robinson, *Jom* **2013**, *65* 1202.

[42] I. Robinson, J. Miao, *MRS Bulletin* **2004**, *29*, 3 177.

[43] J. Miao, T. Ishikawa, I. K. Robinson, M. M. Murnane, *Science* **2015**, *348*, 6234 530.

[44] M. von Laue **1936**, *418* 55.

[45] Y. Gao, X. Huang, H. Yan, G. J. Williams, *Physical Review B* **2021**, *103*, 1 014102.

[46] A. Mokhtar, D. Serban, M. Newton, *Journal of Physics Communications* **2022**, *6*, 5 055003.

[47] I. Robinson, I. Vartaniants, *Applied Surface Science - APPL SURF SCI* **2001**, *182* 186.

[48] M. J. Cherukara, Y. S. Nashed, R. J. Harder, *Scientific reports* **2018**, *8*, 1 16520.

[49] M. Newton, U. Wagner, C. Rau, *Applied Physics Express* **2022**, *15*, 7 077001.

[50] L. Wu, P. Juhas, S. Yoo, I. Robinson, *IUCrJ* **2021**, *8*, 1 12.

[51] D. P. Kingma, J. Ba, Adam: A method for stochastic optimization, **2017**.

[52] A. K. C. Estandarte, C. M. Lynch, M. Monteforte, J. Rawle, C. Nicklin, I. Robinson, *New Journal of Physics* **2018**, *20*, 11 113026.

[53] A. Ulvestad, J. N. Clark, R. Harder, I. K. Robinson, O. G. Shpyrko, *Nano letters* **2015**, *15*, 6 4066.

[54] P. M. Shenai, Z. Xu, Y. Zhao, *Princ. Compon. Anal. Appl* **2012**, 25–40.

[55] W. Hu, R. R. Singh, R. T. Scalettar, *Physical Review E* **2017**, *95*, 6 062122.

[56] E. Mejía-Uriarte, R. Sato-Berrú, M. Navarrete, O. Kolokoltsev, J. Saniger, *Journal of applied research and technology* **2012**, *10*, 1 57.

[57] Y. G. Sinai, *Theory of phase transitions: rigorous results*, volume 108, Elsevier, **2014**.

[58] R. Cowley, *Advances in physics* **1980**, *29*, 1 1.

[59] A. Dobrovolsky, A. Merdasa, E. L. Unger, A. Yartsev, I. G. Scheblykin, *Nature communications* **2017**, *8*, 1 34.

[60] A. Tselev, I. Luk'Yanchuk, I. Ivanov, J. Budai, J. Tischler, E. Strelcov, A. Kolmakov, S. Kalinin, *Nano letters* **2010**, *10*, 11 4409.

[61] H. Guo, K. Chen, Y. Oh, K. Wang, C. Dejoie, S. Syed Asif, O. Warren, Z. Shan, J. Wu, A. Minor, *Nano letters* **2011**, *11*, 8 3207.

[62] R. Basu, P. Magudapathy, M. Sardar, R. Pandian, S. Dhara, *Journal of Physics D: Applied Physics* **2017**, *50*, 46 465602.

[63] R. Shi, J. Wang, X. Cai, L. Zhang, P. Chen, S. Liu, L. Zhang, W. Ouyang, N. Wang, C. Cheng, *The Journal of Physical Chemistry C* **2017**, *121*, 44 24877.